Research Article | Vol. 10, No. 4 / 1 April 2020 / Optical Materials Express 926

Optical Materials EXPRESS

CO_2 laser annealed SiGe core optical fibers with radial Ge concentration gradients

Wei Wu,[1] Mustafa Balci,[1] Seunghan Song,[1] Chunxin Liu,[2] Michael Fokine,[2] Fredrik Laurell,[2] Thomas Hawkins,[3] John Ballato,[3] and Ursula J. Gibson[1,2,*]

[1]Department of Physics and Porelabs, Norwegian University of Science and Technology, Høgskoleringen 5, 7491 Trondheim, Norway
[2]Department of Applied Physics, Royal Institute of Technology, KTH, 10691 Stockholm, Sweden
[3]Department of Materials Science and Engineering, Clemson University, Clemson, SC 29634, USA
*ursula.gibson@ntnu.no

Abstract: CO_2 laser annealing of SiGe core, glass-clad optical fibers is a powerful technique for the production of single-crystal cores with spatially varying Ge concentrations. Laser power, laser scan speed and cooling air flow alter the Ge distribution during annealing. In this work, near-single crystal fibers exhibiting a central axial feature with peak Ge concentration ~15 at% higher than the exterior of the semiconductor core have been prepared. Preferential transmission of near infrared radiation through the Ge-rich region, and spectral data confirm its role as a waveguide within the semiconductor core. This proof-of-concept step toward crystalline double-clad structures is an important advancement in semiconductor core optical fibers made using the scalable molten core method.

1. Introduction

Semiconductor-core optical fibers have numerous potential applications that arise from the fiber's infrared transparency, optoelectronic and nonlinear optical properties [1–5]. These fibers can be made by high pressure chemical vapor deposition within a glass cladding [6,7], or fabrication with the molten core method [8] which is scalable over long lengths and can be used for bulk production [9] of these materials. Silicon core fibers exhibit extraordinary nonlinear optical properties [10–12], and Ge core fibers and compound materials [13,14] are also under development [15–19].

Post fiber-draw processing of the core is of increasing interest. In particular, oven annealing [20], CO_2 laser treatment [7,9,21], and laser-induced tapering [22] have been used to improve the optical transmission for silicon core fiber, and recent results on Ge core material are also promising. Laser treatment of SiGe core fibers has been used to reduce losses [23], to produce single-crystal cores [24], and promote the formation of Janus particles [14]. Thermomigration gathers Ge in the higher temperature region [24,25], and variations in the power and translation velocity of the laser can be used to vary the local composition of the core material, as preferential segregation of the silicon occurs during crystallization. To date, most attention has been placed on variations along the fiber length.

If the temperature gradient can be made radially symmetric, the same process can lead to the formation of compositional features with higher Ge concentration, and thus a higher refractive index, in the center of the core. An elevated concentration of Ge has been observed at the center of SiGe droplets made by rapid solidification processing [26], suggesting that in a cylindrical geometry it should be possible to concentrate Ge along the core axis of this alloy. A Ge-rich region in the center of a graded SiGe rib waveguide has been observed to have lower losses in the near infrared (NIR) [27], making comparable fibers of interest. This is particularly true for applications at wavelengths greater than ~4μm, where the absorption of silica increases rapidly and the cladding could degrade performance of the fiber.

#390482 https://doi.org/10.1364/OME.390482
Journal © 2020 Received 12 Feb 2020; revised 3 Mar 2020; accepted 4 Mar 2020; published 12 Mar 2020

Optical Materials EXPRESS

In this paper, we demonstrate, for the first time to our knowledge, radial compositional structuring of crystalline SiGe fibers and the resultant optical effects, using a commercial 80 W CO_2 laser engraver to form the structures. This is a first step towards scalable fabrication of all-semiconductor, gradient-index cores for long wavelength applications. Although optimal processing has not yet been achieved, these preliminary results demonstrate the potential of laser treatment to create radial gradient structures in alloy fiber with the potential for in-fiber junction and double-clad configurations.

2. Experimental

2.1. Sample preparation

Molten core fabrication [1] of fibers using a conventional draw tower, from a 30 mm outer x 3 mm inner diameter silica preform loaded with high resistivity (>10^3 kΩ-cm) Si and Ge (ρ >50 Ω-cm) produced fiber with cores of 120-150 µm diameter and composition 94 at% Si and 6 at% Ge in an SiO_2 cladding. An alkaline oxide coating between core and silica [28] was used to reduce the interfacial interactions that occur between the core melt and the cladding during drawing at temperatures around 1950 °C, and during subsequent laser annealing. A BRM commercial CO_2 laser engraver with 10.6 µm primary wavelength was used for fiber treatment, as shown in Fig. 1. The fiber was placed at the focal distance (63.5 mm) of the ZnSe lens. Cooling air was directed towards the irradiated surface using a 0.7 mm nozzle, located 3-4 mm from the laser incidence position. The airflow balanced some of the heat load provided by the laser, making the cooling more radially symmetric, and with a tightly focused laser, some removal of cladding material was observed. A series of growth experiments probed the effects of the air pressure and flow, the laser scan velocity and laser power. Samples were polished by hand, placing them in a thick-walled capillary and proceeding through abrasives with 15-0.3 micron grits. In cases where the capillary inner diameter was a poor match to the sample, and the sample short, the endface was polished at an angle to the normal, making the core appear elliptical. Cracks in the core are polishing artifacts, while those in the glass are associated with the fiber drawing process.

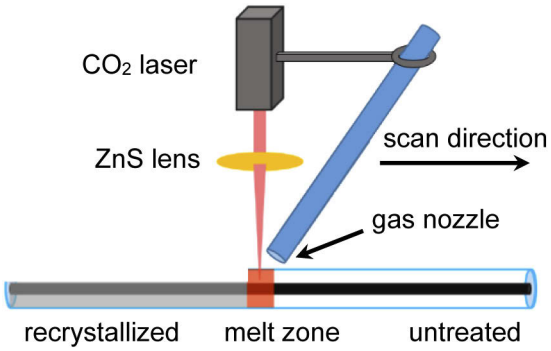

Fig. 1. Fiber annealing setup.

2.2. Optical characterization

Characterization of the optical transmission in the near infrared was made using a 20 mW, 1.55 µm diode laser from QPhotonics that was coupled into the sample using a lensed single mode fiber (SMF) from Oz Optics. The SMF fiber had a nominal working distance of 26 µm for the minimum spot size of 2.5 µm but was used with ~150-200 µm separation from the fiber face to allow complete illumination of the core. An infinity corrected 20x NIR microscope objective from Mitutoyo and a Watec 902H2 NIR camera were placed on the output side of fiber to record

Optical Materials EXPRESS

the image of the transmitted near infrared radiation. A corresponding visible image was obtained by illuminating the exit face of the fiber with white light and using a flip-down mirror to redirect the image (through the same optics) to a conventional USB camera. This permitted determination of the location within the core at which transmission features were observed, for comparison with SEM images. Spectra were acquired with an Energetiq EQ-99 laser driven plasma lamp coupled in through the lensed fiber and out through a 600μm core collection fiber connected to a StellarNet Dwarf-Star spectrometer. Full scale reference values were taken through the silica cladding for determination of the absorption edge of the core.

2.3. Structural and compositional characterization

The fibers were characterized using a scanning electron microscope (Hitachi TM3000) in the backscattered electron mode (BSE) and energy dispersive x-ray spectroscopy (EDS) was performed in a JEOL JSM-840 at 20 kV. A ZEISS ULTRA 55 was used for Electron Backscattered Diffraction (EBSD). X-ray computed tomography (XCT) using a Nikon XT H225STCT allowed imaging of the 3-dimensional compositional structure and visualization of the axial arrangement of the Si and Ge. In both XCT and BSE, heavier elements (in this case Ge) give higher intensity values in images. X-ray diffraction (XRD) was performed using a Bruker DaVinci powder diffractometer with a 15 mm diameter beam from a Mo $K_{\alpha 1,2}$X-ray source (λ=0.7093 Å, 0.7139 Å).

Although it did not give quantitative Ge composition, a histogram of a BSE image used with a threshold function could be used to characterize the relative inhomogeneity of the samples. This method yielded plots with better signal-to-noise than the EDS maps (where a thresholding process has already been applied) and had higher spatial resolution, because of the smaller excitation volume for BSE compared to that for EDS. GIMP software was used to create a histogram of the intensity values of the BSE images of the fiber cores, and to determine the number of pixels with values above that of the uniform Ge concentration background in each sample. Thresholds were typically 115-130 for an 8-bit gray scale. As each pixel is the same size, the percentage of pixels over the threshold intensity gives an area determination of the material with enhanced Ge concentration. Reproducibility of the method was on the order of ±0.5% of the sample area.

3. Results and discussion

The as-drawn fibers showed significant segregation of Ge as seen by others [24] due to constitutional undercooling, but with geometrically oriented features associated with a higher degree of as-drawn crystallinity than previously reported [29]. While the lateral composition has significant structure, the overall composition is uniform averaged over either the cross section or along the length of the fiber. Small variations should be homogenized in the melt zone (~400 μm long) during laser processing. Figure 2(a) is a BSE image of the as-drawn fiber (Table 1, #1), and Fig. 2(b)-(d) are EDS maps for Si, Ge, and O, respectively. Figure 2(e) compares the (unscaled) BSE image brightness to the EDS map intensity values, showing that the analysis of the BSE images is well-correlated with the Ge concentration, but with improved spatial resolution.

3.1. Laser treatment and resultant Ge concentration distribution

Laser treatment experiments were performed to determine the parameters for formation of homogeneous cores as well as those with gradients in the Ge concentration, during the recrystallization process. Table 1 shows test condition for the samples presented here. The effect of air flow, laser scan speed and laser power during the annealing process were studied. The gas flow was varied from 0 to 0.046 L/s, the laser scan speed from 0.3 mm/s to 1.1 mm/s, and the power level was varied between 13.5 and 15.5 W. It was found that laser illumination of 15 W with 0.7 mm/s scan speed, accompanied by gas cooling of 0.041 L/s air flow led to the formation of Ge-rich cores within the SiGe.

Optical Materials EXPRESS

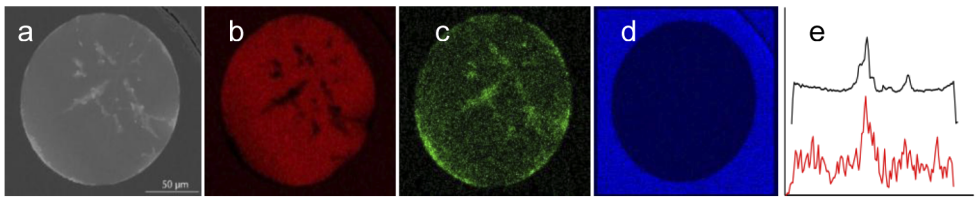

Fig. 2. a) BSE cross-sectional image from an as-drawn fiber. EDX compositional mapping images of: b) Si, c) Ge, and d) O. Scale bar is 50 µm. e) Comparison of BSE brightness (black) vs Ge concentration from EDS map (red), in a narrow rectangle that crosses the center of the fiber from left to right.

Table 1. Annealing conditions for samples

Sample #	air flow (L/s)	laser scan velocity (mm/s)	laser power (W)
1	As drawn		
2	0	0.7	14.5
3	0.034	0.7	14.5
4	0.046	0.7	14.5
5	0.041	0.3	14.5
6	0.041	0.5	14.5
7	0.041	0.9	14.5
8	0.041	1.1	14.5
9	0.041	0.7	13.5
10	0.041	0.7	14
11	0.041	0.7	15
12	0.041	0.7	15.5
15	0.041	0.7	14.5
16	0.041	0.7	14.5

3.1.1. Laser power

Figure 3 shows BSE images of fibers annealed for fixed translation speed and airflow, with different laser powers. For 13.5 W (Fig. 3(a)) and 14 W (Fig. 3(b)), the laser power was too low to melt the entire core, and a Ge composition gradient was formed, with a peak on the laser-heated side. The gradient forms due to thermomigration of Ge-rich droplets to the highest temperature, under the influence of the lateral temperature difference. During cooling of this partial-core laser-induced melting, Si-rich material precipitated first at the distal side of the liquid (partway through the core), and Ge-rich melt, with a lower melting point, solidified last, on the side where the laser was incident (red arrows) [24,30]. For the higher power annealing in Figs. 3(c) and 3(d), the entire core was melted, and the Ge-rich features of the as-drawn fiber were modified. For 15 W (Fig. 3(c)), there was a slightly elevated Ge content away from the edges, and for the highest power, the fiber core was homogeneous. At this power, the airflow cooling was insufficient to maintain a radial thermal gradient.

EDS data in Fig. 3(e) confirmed the presence of the Ge-rich surface feature and showed that in the vicinity of the position value 100 µm there were elevated Ge concentrations. These features are attributed to the solidification proceeding from the outside to the inside of the core. Figure 3(f) (14 W) shows that the intensity values of the image, while not calibrated, can be used for an assessment of high Ge concentration with higher resolution than EDS. Further Ge inhomogeneity studies in this paper used BSE images.

Optical Materials EXPRESS

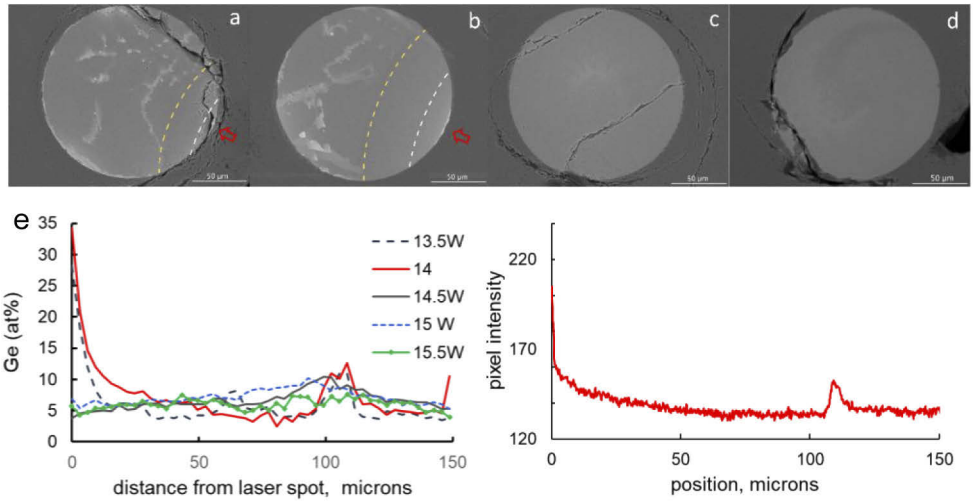

Fig. 3. SEM images of cross-sections of cores for fibers annealed with laser power of a) 13.5 W (#9), b) 14 W (#10), c) 15 W (#11) and d) 15.5 W (#12). The Ge 8 at% and 4 at% boundaries are marked with white and yellow arcs in a) and b) and the red arrows show the laser incidence position. e) Line scan of Ge concentration along the diameter from the laser incidence point, and f) pixel intensity along the path characterized by EDS for the 14 W scan.

3.1.2. Laser scan speed

The scanning speed of the laser beam is a factor in solidification stability of alloys where constitutional undercooling can occur [24], and can also affect elemental distribution [31]. For slow laser scan rates (and hence solidification speed), and large thermal gradients [32], the solidification front is stable. If the speed exceeds a critical value, non-planar growth results. For a radially dominated cooling process, a high transverse scan speed can lead to the formation of a concave crystallization front in a cylindrical geometry [33, 34] and the large surface-to-volume ratio of a fiber may be expected to enhance this effect. BSE images in Fig. 4(a)-(d) show the elemental segregation as the scan speed is increased from 0.3 to 1.1 mm/s. At the lowest speed, the fiber is homogeneous. For Fig. 4(b) (0.5 mm/s), there is a slight increase in the Ge content towards the middle of the fiber, suggesting radial cooling. For Figs. 4(c) and 4(d), the growth front becomes unstable, as it is for the as-drawn fibers. At all speeds, USB camera images showed that the full core diameter was melted. Figure 4(e), based on the image brightness, indicates that the Ge content becomes more inhomogeneous at higher laser scan speeds, as expected for SiGe alloys [24,35].

3.1.3. Air flow

Air flow incident on the fiber in the laser heated region both increases gas transport of thermal energy and removes vaporized silica, two mechanisms that can balance the directional heating of the laser. BSE images in Fig. 5(a-c) show the effect of air flow during SiGe fiber annealing. At intermediate values, the airflow cooling balanced the directional heating provided by the laser and increased the radial temperature gradient sufficiently to form Ge-rich regions within the core, rather than at the surface. For 0.034 L/s (Fig. 5(b)), there is a region of concentrated Ge, while in Fig. 5(c), there is a slightly elevated Ge concentration in the central part of the fiber, similar to that observed for the scan speed of 0.5 mm/s. The homogeneous material around the periphery of the fiber has a low Ge content and suggests radial cooling. The low Ge content in this region is

Optical Materials EXPRESS

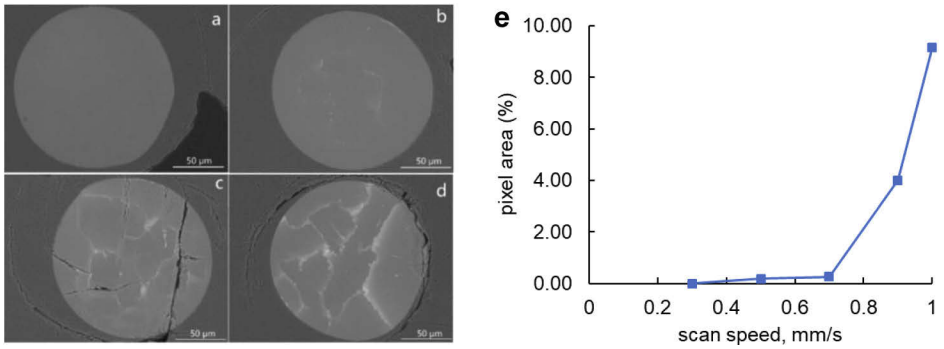

Fig. 4. SEM images of cross-sections of fibers annealed with laser scan speeds of a) 0.3 mm/s (#5), b) 0.5 mm/s (#6), c) 0.9 mm/s (#7), and d) 1.1 mm/s (#8). e) Area of above average intensity in BSE image as a function of scan speed.

consistent with Scheil-Gulliver modeling [36], where the first-to-solidify material is deficient in the component with the lower melting point. Figure 5(d) is a plot of the number of above average intensity pixels in the image of the fiber, and shows that for higher airflow, high Ge concentrations are limited to a small area of the fiber cross-section. Figures 5(e) and 5(f) are top and side view photomicrographs of fibers annealed without (upper) and with airflow. The hazy surface of the (upper) fiber made without air assist is redeposited silica; with airflow, this material is removed.

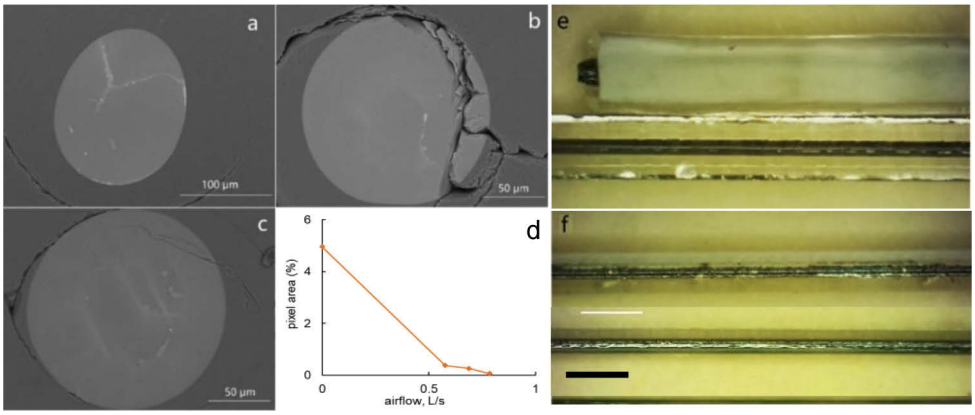

Fig. 5. SEM images of cross-sections of fibers annealed with various air flow values (a) sample # 2 (0 L/s) (b) sample #3 (0.034 L/s) (c) sample #4 (0.046 L/s) (d) area of Ge-rich regions as a function of air pressure. Scale bars 100, 50, 50 µm. Microscope images for sample #2 (above) and #15 (0.041 L/s) below; top (e) and side views (f) are shown. Scale bar 650 µm. .

3.1.4. Ge-rich central features

If the cooling of the fiber is radially symmetric (or nearly so), the preferential solidification of silicon on the exterior surface can result in high-concentration Ge-rich filaments along the axis of the silicon core. Figure 6(a) is a BSE cross-sectional image of sample #15, made with 14.5 W of laser power, 0.7 mm/s scan speed and 0.041 L/s of airflow. With these conditions, we observe an axial high Ge content region, slightly offset from the center of the core (image contrast adjusted to make the core feature more prominent). Figure 6(b) is an XCT cross-sectional image

Optical Materials EXPRESS

of the fiber, showing partial removal of the glass, and bright central region within the core, also indicating a high Ge content. Figure 6(c) is a transverse XCT scan that shows that the Ge-rich filament extends along the core through the entire annealed length. Considering the complicated compositional distribution of the as-drawn fiber, imperfections in the structure formed are not unexpected. Figure 6(d) is an XCT image of a fiber made with pulsed airflow, confirming the role of the airflow in balancing the heating and cooling processes.

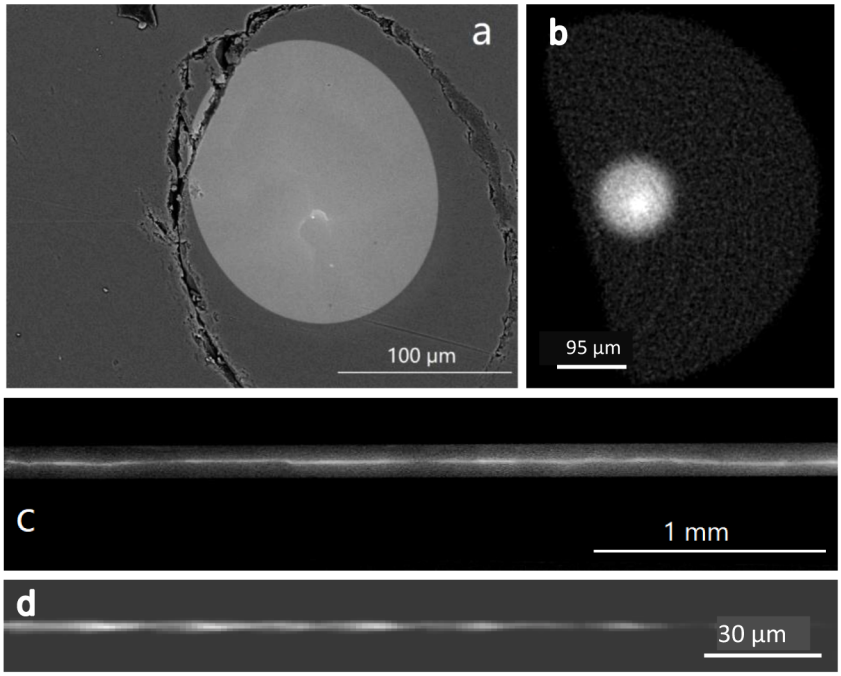

Fig. 6. Ge-rich core samples (a) BSE image of fiber #15 (cracks from end-face polishing and stress at the margins of the glass modified by the interface layer) (b) XCT cross section and (c) side view. Fiber #16: (d) XCT of fiber showing features resulting from the periodic variations in airflow with a compressor.

Figure 7 shows analysis results for another fiber (#16) made under the same conditions as sample #15; Fig. 7(a) is a BSE image showing a similar Ge-rich core. Some Ge-rich liquid fails to reach the center of the fiber resulting in Ge "tendrils". However, the Ge content in these regions is typically only 2% above the background concentration according to EDS line scans, or an eighth of the difference observed for the Ge-rich core. Figure 7(b) is an EBSD map of the cross section of fiber showing two slightly different crystal orientations indicating a low-angle grain boundary. As shown in Fig. 7(c), the EDS-reported concentration of the in the Ge-rich region is ~22 at%, and the EDS- determined diameter of the Ge-rich region is approximately 3 µm. It should be noted that this is close to the resolution limit for EDS in this instrument, and the actual radius may be less (with a correspondingly higher concentration). The full width at half maximum (FWHM) of the feature in the BSE image is 1.5 µm, suggesting almost pure Ge in the core. Figure 7(d) is XRD data for as-drawn and annealed fibers, showing the high degree of crystalline order induced by the annealing process, indicated by the reduced number of Bragg peaks observable [31].

A Ge concentration of 22 at% in the Ge-rich region and 7 at% in the surrounding core would give an index difference of approximately 0.06 at 1.55 µm [37], forming a waveguide within the silicon core. The transmission of sample #15, with length of 7 mm, was characterized, and

Optical Materials EXPRESS

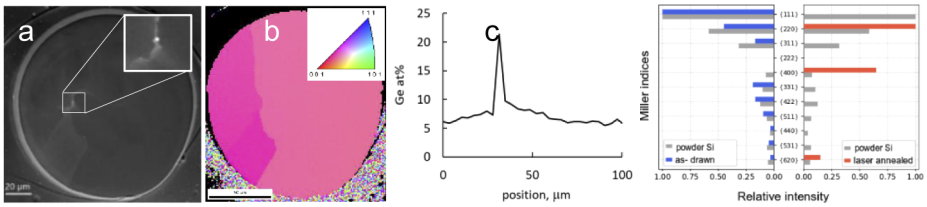

Fig. 7. SEM and EBSD images of cross-sections of Ge-rich core fiber #16. (a) BSE SEM image of the fiber (b) EBSD map of the silicon showing a single low-angle grain boundary (inset: orientation map) (c) EDS line scan of the Ge concentration. d) X-ray diffraction of an as-drawn and laser-annealed fiber from the same production run.

shows preferred transmission in the high index, high Ge region. Figure 8(a) is an IR camera image with the illumination fiber drawn back from the fiber core to highlight defects in the glass cladding (to assist with image alignment), and Fig. 8(b) shows a visible image of the output face, confirming the outline of the semiconductor core. The input fiber was then positioned to illuminate the full core, but not the glass cladding. The image from the NIR camera (threshold used to reduce noise) in Fig. 8(c) shows preferential transmission of the 1.55µm laser diode through the Ge-rich area of the core. Figure 8(d) is the BSE image of the exit face, with intensity indicating higher Ge concentration; the high transmission features of the NIR camera image are clearly associated with the location of the Ge-rich material. In order to confirm the waveguiding role of the Ge-rich material, spectral data was acquired with a broadband source illuminating the core. The spectrum transmitted through the 9 mm long Ge-rich core sample (#15) is shown with normalized transmission values for a silicon core fiber (5 mm long) and a homogeneous, annealed SiGe core fiber (8.5 mm long) in Fig. 8(e). In each case, the full diameter of the core was illuminated. The longer wavelength absorption edge of sample #15 confirms that the Ge-rich filament guides the light preferentially within the SiGe core. Signal levels for the Ge core sample were lower than for the other fibers, presumably due to the imperfection of the core, and inefficient coupling.

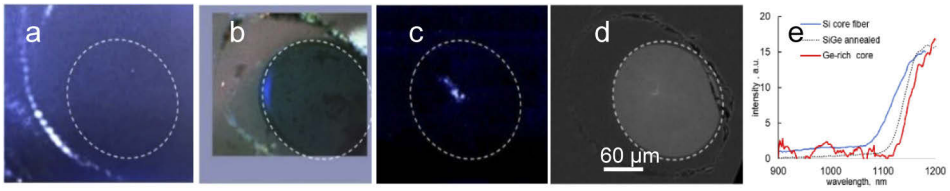

Fig. 8. Images of a) off-axis illuminated cladding, highlighting glass cracks, b) visible image of exit face of fiber, c) 1.55 µm illumination of the core showing preferential transmission through the Ge-rich region and d) contrast enhanced SEM micrograph showing the location of the high-Ge region. e) The spectrum transmitted through the fibers. White dashed circles show outline of the core; scale bar 60 µm.

4. Modeling

There are three stages during directional solidification of SiGe alloy samples in the absence of convection and when limited diffusion prevents formation of a homogeneous material; an initial transient with a lower concentration of Ge, a steady state, and a final Ge-enriched transient. At the start of the solidification process, Si solidifies preferentially, and excess Ge is rejected into the melt. There is then a steady-state growth where the excess Ge at the solidification front results in material with average alloy composition [24]. The approximate width of the Ge-rich liquid at

Optical Materials EXPRESS

the front is given by δ= D/V, where D is the diffusion coefficient and V is the velocity of the solidification front. When the relative motion of the fiber and heat source ceases, a terminal transient is formed as the excess Ge solidifies [38] at a lower temperature than for the other regions due to the lower melting point of the Ge. More detailed modeling of the fibers including radial and axial temperature gradients predict that the Ge rich region should have a radius on the order of 1 μm; a simplified limiting case is presented here.

For purely radial cooling of a cylindrical sample, the initial preferential Si solidification would move Ge from the surface and deposit this excess at the center of the sample. An upper bound on the Ge-rich core for this case can be made by assuming that the excess Ge gathered in the initial transient is all deposited in the center of the fiber in the final transient, as pure Ge. The initial transient will contribute $2\pi R\delta\Delta C$, where ΔC is the excess Ge at the liquid interface; R is the outer radius of the core, and δ is the width of the transient, given by D/V, with D the diffusion coefficient (1x 10^{-4} cm^2/s [39, 40]), and V the velocity of the phase front (0.7 mm/s). The value of ΔC was approximated as [(C_0/k)-C_0], where C_0 is the initial concentration (6%), and k=0.23 is the equilibrium partition coefficient [41]. If this material forms a terminal transient as a cylinder of pure Ge at the center of the core, the radius of the Ge region will be

$$r = \sqrt{\frac{2RD}{V}\Delta C} \tag{1}$$

With the fiber core radius (R=75 μm), we get a value of ~20 μm as the maximum (pure) Ge core diameter. This is an overestimate in several regards; the distance to reach equilibrium in a traveling melt zone is generally taken to be $4D/(V\mathrm{k})$, which is comparable to the core diameter, and the gradients are not purely radial. For a translating fiber, there will be both axial and radial temperature gradients, and central features are only expected if a concave growth front can be established. If the translation speed is too low (making the axial gradient dominant), the heating is uneven, or the diffusion is limited due to a low temperature, a smaller Ge-rich region will be expected. The exact dynamics are complicated, because the thermal conductivity, the diffusion and solidification temperatures will all be affected by local concentration of Ge. However, the order of magnitude agreement of this simple model is encouraging.

5. Conclusion

Production of a Ge-rich central feature within a SiGe crystalline-core optical fiber, and the potential for improved optical performance based on this structure have been demonstrated. Formation of coaxial concentration gradient requires that fiber cooling should be predominantly radial, and rapid enough to promote significant segregation, but not so rapid that the critical velocity is exceeded [25,35]. The airflow used in conjunction with the CO_2 laser in these experiments increased the cooling rate, and with an appropriate balance of airflow, power and translational velocity, provided the necessary radial cooling. The power value was set to melt the entire core without overwhelming the cooling effect of the airflow, and the translation was balanced between the requirements of high speed to promote a concave growth front, and low speed to assure that the critical velocity was not exceeded. Limited experiments utilizing systems with symmetric CO_2 beams, but without airflow, have not yet resulted in the observation of core features, suggesting the importance of forced convection. Large cores make it easier to establish a radial thermal gradient large enough to drive segregation of the Ge; for small core fibers, a higher translation velocity, and faster surface cooling will be needed to form the conical solidification front believed to be responsible for the observations here.

Optical transmission measurements on these structured SiGe fibers show preferential transmission of a 1.55μm diode laser through the Ge-rich filament due to the local refractive index gradient. The spectrum from a broadband source transmitted through the fiber supports this observation; the Ge-rich region is acting as the core of a semiconductor-clad region. Such fibers

Optical Materials EXPRESS

could reduce waveguide losses for IR applications beyond 4 microns, where silica cladding is absorptive. Similar structures in SiGe fibers with higher Ge compositions should allow extension of the IR transmission range; further research to find the optimum processing conditions is warranted.

Funding

Norges Forskningsråd (245963, 262232, 262644); Vetenskapsrådet (2016-04488); Stiftelsen för Strategisk Forskning (RMA15-0135); Knut och Alice Wallenbergs Stiftelse (2016.0104); J.E. Sirrine Foundation.

Disclosures

The authors declare no conflicts of interest.

References

1. J. Ballato, T. Hawkins, P. Foy, B. Yazgan-Kokuoz, C. McMillen, L. Burka, S. Morris, R. Stolen, and R. Rice, "Advancements in semiconductor core optical fiber," Opt. Fiber Technol. **16**(6), 399–408 (2010).
2. R. He, T. D. Day, M. Krishnamurthi, J. R. Sparks, P. J. A. Sazio, V. Gopalan, and J. V. Badding, "Silicon p-i-n junction fibers," Adv. Mater. **25**(10), 1461–1467 (2013).
3. J. R. Sparks, R. He, N. Healy, M. Krishnamurthi, A. C. Peacock, P. J. A. Sazio, V. Gopalan, and J. V. Badding, "Zinc Selenide Optical Fibers," Adv. Mater. **23**(14), 1647–1651 (2011).
4. L. Lagonigro, N. Healy, J. R. Sparks, N. F. Baril, P. J. A. Sazio, J. V. Badding, and A. C. Peacock, "Low loss silicon fibers for photonics applications," Appl. Phys. Lett. **96**(4), 041105 (2010).
5. K. Sui, X. Feng, Y. Hou, Q. Zhang, S. Qi, Y. Wang, and P. Wang, "Glass-clad semiconductor germanium fiber for high-speed photodetecting applications," Opt. Mater. Express **7**(4), 1211 (2017).
6. J. R. Sparks, P. J. A. Sazio, V. Gopalan, and J. V. Badding, "Templated chemically deposited semiconductor optical fiber materials," Annu. Rev. Mater. Res. **43**(1), 527–557 (2013).
7. X. Ji, S. Lei, S.-Y. Yu, H. Y. Cheng, W. Liu, N. Poilvert, Y. Xiong, I. Dabo, S. E. Mohney, J. V. Badding, and V. Gopalan, "Single-crystal silicon optical fiber by direct laser crystallization," ACS Photonics **4**(1), 85–92 (2017).
8. J. Ballato, T. Hawkins, P. Foy, R. Stolen, B. Kokuoz, M. Ellison, C. McMillen, J. Reppert, A. M. Rao, M. Daw, S. Sharma, R. Shori, O. Stafsudd, R. R. Rice, and D. R. Powers, "Silicon optical fiber," Opt. Express **16**(23), 18675–18683 (2008).
9. N. Healy, M. Fokine, Y. Franz, T. Hawkins, M. Jones, J. Ballato, A. C. Peacock, and U. J. Gibson, "CO_2 laser-induced directional recrystallization to produce single crystal silicon-core optical fibers with low loss," Adv. Opt. Mater. **4**(7), 1004–1008 (2016).
10. A. C. Peacock, P. Mehta, L. Shen, F. H. Suhailin, N. Vukovic, and N. Healy, *Silicon Fibre Devices for Nonlinear Applications* (IEEE, 2014).
11. A. C. Peacock, J. Campling, A. F. J. Runge, H. Ren, L. Shen, O. Aktas, P. Horak, N. Healy, U. J. Gibson, and J. Ballato, "Wavelength conversion and supercontinuum generation in silicon optical fibers," IEEE J. Sel. Top. Quantum Electron. **24**(3), 1–9 (2018).
12. P. Mehta, N. Healy, T. D. Day, J. R. Sparks, P. J. A. Sazio, J. V. Badding, and A. C. Peacock, "All-optical modulation using two-photon absorption in silicon core optical fibers," Opt. Express **19**(20), 19078 (2011).
13. S. Song, N. Healy, S. K. Svendsen, U. L. Österberg, A. V. C. Covian, J. Liu, A. C. Peacock, J. Ballato, F. Laurell, M. Fokine, and U. J. Gibson, "Crystalline GaSb-core optical fibers with room-temperature photoluminescence," Opt. Mater. Express **8**(6), 1435–1440 (2018).
14. S. Chaudhuri, X. Ji, H.-T. Huang, T. Day, V. Gopalan, J. Badding, and J. Badding, "Small core SiGe alloy optical fibers by templated deposition," in *Conference on Lasers and Electro-Optics (2017)*, Paper JW2A.69 (Optical Society of America, 2017), p. JW2A.69.
15. J. Ballato, T. Hawkins, P. Foy, B. Yazgan-Kokuoz, R. Stolen, C. McMillen, N. K. Hon, B. Jalali, and R. Rice, "Glass-clad single-crystal germanium optical fiber," Opt. Express **17**(10), 8029 (2009).
16. J. Ballato, T. Hawkins, P. Foy, S. Morris, N. K. Hon, B. Jalali, and R. Rice, "Silica-clad crystalline germanium core optical fibers," Opt. Lett. **36**(5), 687–688 (2011).
17. X. Ji, R. L. Page, S. Chaudhuri, W. Liu, S.-Y. Yu, S. E. Mohney, J. V. Badding, and V. Gopalan, "Single-crystal germanium core optoelectronic fibers," Adv. Opt. Mater. **5**(1), 1600592 (2017).
18. M. Ordu, J. Guo, B. Tai, M. K. Hong, S. Erramilli, S. Ramachandran, and S. N. Basu, "Mid-infrared transmission through germanium-core borosilicate glass-clad semiconductor fibers," Opt. Mater. Express **7**(9), 3107–3115 (2017).
19. J. Shi, F. Han, C. Cui, Y. Yu, and X. Feng, "Mid-infrared dielectric-metal-semiconductor composite fiber," Opt. Commun. **459**, 125093 (2020).
20. S. Chaudhuri, J. R. Sparks, X. Ji, M. Krishnamurthi, L. Shen, N. Healy, A. C. Peacock, V. Gopalan, and J. V. Badding, "Crystalline Silicon Optical Fibers with Low Optical Loss," ACS Photonics **3**(3), 378–384 (2016).

Optical Materials EXPRESS

21. Z. Zhao, Y. Mao, L. Ren, J. Zhang, N. Chen, and T. Wang, "CO_2 laser annealing of Ge core optical fibers with different laser power," Opt. Mater. Express **9**(3), 1333 (2019).
22. Y. Franz, A. F. J. Runge, H. Ren, N. Healy, K. Ignatyev, M. Jones, T. Hawkins, J. Ballato, U. J. Gibson, and A. C. Peacock, "Material properties of tapered crystalline silicon core fibers," Opt. Mater. Express **7**(6), 2055–2061 (2017).
23. T. Sørgård, K. Mühlberger, W. Wu, X. Yang, T. Hawkins, J. Ballato, F. Laurell, M. Fokine, U. J. Gibson, and U. J. Gibson, "Reduced loss in SiGe-core optical fibers," in *Conference on Lasers and Electro-Optics (2018)*, Paper SF3I.6 (Optical Society of America, 2018), p. SF3I.6.
24. D. A. Coucheron, M. Fokine, N. Patil, D. W. Breiby, O. T. Buset, N. Healy, A. C. Peacock, T. Hawkins, M. Jones, J. Ballato, and U. J. Gibson, "Laser recrystallization and inscription of compositional microstructures in crystalline SiGe-core fibres," Nat. Commun. **7**(1), 13265 (2016).
25. A. Gumennik, E. C. Levy, B. Grena, C. Hou, M. Rein, A. F. Abouraddy, J. D. Joannopoulos, and Y. Fink, "Confined in-fiber solidification and structural control of silicon and silicon–germanium microparticles," Proc. Natl. Acad. Sci. U. S. A. **114**(28), 7240–7245 (2017).
26. N. Hussain, A. M. Mullis, and N. Haque, "Effect of cooling rate on the microstructure of rapidly solidified SiGe," Mater. Charact. **154**, 377–385 (2019).
27. J. M. Ramirez, V. Vakarin, J. Frigerio, P. Chaisakul, D. Chrastina, X. L. Roux, A. Ballabio, L. Vivien, G. Isella, and D. Marris-Morini, "Ge-rich graded-index $Si_{1-x}Ge_x$ waveguides with broadband tight mode confinement and flat anomalous dispersion for nonlinear mid-infrared photonics," Opt. Express **25**(6), 6561–6567 (2017).
28. E. F. Nordstrand, A. N. Dibbs, A. J. Eraker, and U. J. Gibson, "Alkaline oxide interface modifiers for silicon fiber production," Opt. Mater. Express **3**(5), 651–657 (2013).
29. M. Balci, "Production of single crystal semiconductor core optical fibers," Trondheim, Norway (November 23, 2019).
30. S. Song, K. Lønsethagen, F. Laurell, T. W. Hawkins, J. Ballato, M. Fokine, and U. J. Gibson, "Laser restructuring and photoluminescence of glass-clad GaSb/Si-core optical fibres," Nat. Commun. **10**(1), 1790 (2019).
31. S. M. Yoon and I. N. Miaoulis, "Effect of scanning speed on the stability of the solidification interface during zone-melting recrystallization of thin silicon films," J. Appl. Phys. **72**(1), 316–318 (1992).
32. S. M. Yoon and I. N. Miaoulis, "Solidification front stability during zone-melting recrystallization of thin silicon films," J. Cryst. Growth **126**(2-3), 275–284 (1993).
33. F. L. Mota, N. Bergeon, D. Tourret, A. Karma, R. Trivedi, and B. Billia, "Initial transient behavior in directional solidification of a bulk transparent model alloy in a cylinder," Acta Mater. **85**, 362–377 (2015).
34. M. Ordu, J. Guo, A. E. Akosman, S. Erramilli, S. Ramachandran, and S. N. Basu, "Effect of thermal annealing on mid-infrared transmission in semiconductor alloy-core glass-cladded fibers," *Adv. Fiber Mater.* (2020).
35. W. A. Tiller, K. A. Jackson, J. W. Rutter, and B. Chalmers, "The redistribution of solute atoms during the solidification of metals," Acta Metall. **1**(4), 428–437 (1953).
36. G. H. Gulliver, "The quantitative effect of rapid cooling upon the constitution of binary alloys," *J. Inst. Met.* **9** (1913).
37. J. Humlíček, A. Röseler, T. Zettler, M. G. Kekoua, and E. V. Khoutsishvili, "Infrared refractive index of germanium–silicon alloy crystals," Appl. Opt. **31**(1), 90–94 (1992).
38. W. Wu, M. H. Balci, K. Mühlberger, M. Fokine, F. Laurell, T. Hawkins, J. Ballato, U. J. Gibson, and U. J. Gibson, "Ge-capped SiGe core optical fibers," Opt. Mater. Express **9**(11), 4301–4306 (2019).
39. H. Weis, F. Kargl, M. Kolbe, M. M. Koza, T. Unruh, and A. Meyer, "Self- and interdiffusion in dilute liquid germanium-based alloys," J. Phys.: Condens. Matter **31**(45), 455101 (2019).
40. H. Miyata, S. Adachi, Y. Ogata, T. Tsuru, Y. Muramatsu, K. Kinoshita, O. Odawara, and S. Yoda, "Crystallographic investigation of homogeneous SiGe single crystals grown by the traveling liquidus-zone method," J. Cryst. Growth **303**(2), 607–611 (2007).
41. H. Y. S. Koh, *Rapid Melt Growth of Silicon Germanium for Heterogeneous Integration on Silicon* (Stanford University, 2011).